Supporting Information

Gut microbiota-driven, acid-free recovery and upcycling of spent lithium-ion battery cathodes

Min Li[a,b,#], Danni Zhang[b,#], Di Na[c], Pan Liu[b], Qiuli Xia[b], Yaojie Yu[b], Xianjun Guan[d], Fengjian Liu[e], Tingyue Gu[f], Gege Gu[g], Chong Seung Yoon[h,i,]* Yongqiang Fan[a,b,]*, Dake Xu[b,]*

[a] College of Life and Health Sciences Northeastern University, Shenyang, 110819, China

[b] State Key Laboratory of Digital Steel, School of Materials Science and Engineering, Northeastern University, Shenyang, 110819, China

[c] Department of Surgical Oncology and General Surgery, The First Hospital of China Medical University, Shenyang, 110001, China

[d] Shi-changxu Innovation Center for Advanced Materials, Institute of Metal Research, Chinese Academy of Sciences, Shenyang 110016, China

[e] Liaoning Provincial Institute of Metrology, Shenyang 110004, China

[f] Department of Chemical and Biomolecular Engineering, Institute for Corrosion and Multiphase Technology, Ohio University, Athens, OH 45701, USA

[g] Instrumental Analysis Center of Dalian University of Technology, Dalian, 116024, China

[h] Department of Materials Science and Engineering, Hanyang University, Seoul 04763, South Korea

[i] Department of Battery Engineering, Hanyang University, Seoul 04763, South Korea

* Corresponding author (Chong Seung Yoon), e-mail: csyoon@hanyang.ac.kr.

*Corresponding author (Yongqiang Fan), e-mail: fanyongqiang@mail.neu.edu.cn.

* Corresponding author (Dake Xu), e-mail: xudake@mail.neu.edu.cn.

[#] Both authors contribute equally to this paper

Number of pages: 23

Number of tables: 4

Number of figures: 13

Section 1

Synthesis methods for $NH_4CoPO_4 \cdot H_2O$ and $NH_4MnPO_4 \cdot H_2O$

$NH_4CoPO_4 \cdot H_2O$ was prepared according to the method reported by Wang et al[1]. Briefly, 3.0 g of ammonium phosphate was added to a beaker with 20 mL deionized (DI) water and 20 mL polyethylene glycol 600 (PEG 600). The mixture was stirred at room temperature until the solid completely dissolved. Then, 0.2 g of cobalt chloride was added into the solution with vigorous magnetic stirring at room temperature for 4 h. The obtained homogeneous purple-colored precipitates were washed several times with DI water and pure ethanol, and then dried at 50°C in the air to obtain a purple powder.

$NH_4MnPO_4 \cdot H_2O$ was prepared according to the method reported by Pang et al[2]. In this work, 3.0 g of ammonium chloride and 0.2 g of ammonium phosphate was added to a beaker together with 20 mL DI water and 20 mL glycerol. The mixture was stirred at room temperature until the solids were completely dissolved. Then, 0.2 g $MnCl_2 \cdot 4H_2O$ was added to solution, and the mixture was stirred with vigorous magnetic stirring at room temperature for 12 h. The obtained homogeneous white precipitates were washed several times with DI water and pure ethanol before being dried at 40°C to obtain a white powder.

Section 2

Detailed spectral fitting and interpretation provided

X-ray photoelectron spectroscopy (XPS) and absorption near-edge structure (XANES) spectra results (Fig. 6) confirmed that the metal ions dissolution process was accompanied by redox reactions. After exposure to gut microbiota, the proportions of Ni(II), Co(II), and Mn(II) in the residues increased significantly (Fig. 6a–c), indicating that gut microbiota promoted metal reduction. For example, in the spent battery powder, Ni(III) and Ni(II) accounted for 32.2% ($2p_{3/2}$ BE at 857.4 eV) and 34.6% ($2p_{3/2}$ BE at 855.6 eV), respectively (Fig. 6a and Supplementary Table S2). In contrast, the residues following interactions with gut microbiota showed a reduced fraction of Ni(III) at 28.6% ($2p_{3/2}$ BE = 857.9 eV), accompanied by an elevated Ni(II) fraction of 40.9% ($2p_{3/2}$ BE = 855.7 eV).

Similar changes occurred for Co: the spent battery powder contained 47.6% Co(III) ($2p_{3/2}$ BE = 781.1 eV) and 18.1% Co(II) ($2p_{3/2}$ BE = 781.4 eV), whereas the residues after interaction with gut microbiota contained 32.3% Co(III) ($2p_{3/2}$ BE = 781.1 eV) and 33.7% Co(II) ($2p_{3/2}$ BE = 782.6 eV) (Fig. 6b and Supplementary Table S2). The Mn 2p spectra exhibited broad and asymmetric peaks, arising from signal overlaps among Mn(II), Mn(III), and Mn(IV), which posed difficulties in evaluating the oxidation states solely from these spectra (Fig. 6c and Supplementary Table S2). Nevertheless, the Mn 3s peak splitting energy (ΔE) decreased as the average oxidation state rose, offering a reliable approach for determining the Mn valence states[3]. The correlation is expressed as: average valence state = $8.95 - 1.13\Delta E$[4]. In the spent NCM523 powder and the residues after gut microbiota incubation, the ΔE values were 4.62 eV and 5.86 eV, respectively, corresponding to average Mn valence states of 3.73 and 2.33 (Fig. 6c). The average Mn valence state was significantly lower in the residues after gut microbiota incubation compared to that in the spent NCM523 powder. According to the XPS results (Fig. 6d and Supplementary Table S2), the spent NCM523 powder contained 25.7% Mn(IV) ($2p_{3/2}$ BE = 643.5 eV) and 40.8% Mn(III) ($2p_{3/2}$ BE = 642.1 eV). In contrast, the residues after incubation with gut microbiota contained 41.0% Mn(II) ($2p_{3/2}$ BE = 640.6 eV), and Mn(IV) were no longer detectable in the residues.

XPS can detect the oxidation state of each element on the sample surface, while the data based on XANES results are capable of providing the specific percentage of different phases in the sample bulk through linear combination fitting (LCF) treatment. The results were shown in Fig. 6e–h.

The secondary minerals formed in the residues (Fig. 5a) showed that both Co and Mn exist in low-valent states (Co(II), Mn(II)), and this distinct valence change is also clearly verified by

XANES spectra (Fig. 6e–h), which is consistent with the XPS results. The Co *K*-edge XANES analysis (Fig. 6e) revealed that the absorption edges of Co_2O_3, CoO, $CoCO_3$, and $NH_4CoPO_4·H_2O$ standards were located at 7729.4 eV, 7725.9 eV, 7723.6 eV, and 7723.7 eV, respectively, similar to previous studies[5-7]. In the untreated spent battery powder, the Co absorption edge was located at 7728.3 eV, close to that of Co_2O_3, indicating the bulk battery powder contained Co(III). The absorption edge of Co in the residues was located at 7726.0 eV, indicating that the bulk residues predominantly contained Co(II). LCF analysis (Fig. 6f and Supplementary Table S3) indicated that the residues retained 11.0% untreated battery structure, with other phases identified as 24.3% $NH_4CoPO_4·H_2O$, 30.0% CoO, 25.7% Co_2O_3, and 8.9% $CoCO_3$-like phase. The LCF results reveal that in addition to $NH_4CoPO_4·H_2O$ (24.3%) phases, a $CoCO_3$-like phase accounts for 8.9% of the Co-bearing phases in the residues. The results were consistent to some extent with the XRD data. The Mn *K*-edge XANES spectra (Fig. 6g) indicated that the absorption edges of MnO_2, Mn_2O_3, MnO, $MnCO_3$, and $NH_4MnPO_4·H_2O$ standards were located at 6561.3 eV, 6558.3 eV, 6554.9 eV, 6551.1 eV and 6552.1 eV, respectively, consistent with previous studies[7,8]. The absorption edge of Mn in the untreated spent battery powder mainly corresponded closely resembles that of MnO_2, indicating that Mn in the untreated bulk material exists predominantly in the +4.0 oxidation state.

In the residues, the Mn absorption edges shifted to lower energies, indicating the reduction of Mn(IV) to the low-valent states (Mn(II) and Mn(III)). In addition, a small peak located at 6559.4 eV indicated that Mn(IV) still existed in the bulk residues. LCF quantitative analysis (Fig. 6h and Supplementary Table S3) revealed that only 3.8% of Mn remained as the untreated battery structure. The residues were predominantly composed of 43.8% $NH_4MnPO_4·H_2O$, 30.7% Mn_2O_3, and 9.8% a $MnCO_3$-like phase, along with minor fractions of 7.5% MnO_2 and 1.9% MnO. The results were in agreement with the XPS data to some extent, further highlighting the reducing capability of the gut microbiota. It should be emphasized that $CoCO_3$-

like and $MnCO_3$-like phases were not detected by XRD analysis. Typically, one reason for the absence of those diffraction peaks belonging to these two minerals is the unsatisfactory detection limit of XRD for minor phases in multicomponent systems ($\leq 5\%$)[9,10]. However, given that the carbonate contents quantified by LCF exceeded this threshold, the absence of corresponding XRD peaks indicates that $CoCO_3$ and $MnCO_3$ likely exist in poorly crystalline states. Therefore, the bulk-sensitive XANES data were presented here to facilitate more accurate analysis of the phase composition in the residues and to give reliable evidence about the redox dissolution mechanism involved in this study.

Table S1. List of standard equations representing the dissolution behavior of metal[11,12].a)

Equation	**Comment**
$X = K_c t$	Film diffusion control dense constant size small particles-all geometries
$1 - (1 - X)^{2/3} = K_c t$	Film diffusion control dense shrinking spheres
$1 - (1 - X)^{1/2} = K_c t$	Chemical reaction control dense constant size cylindrical particles
$1 - (1 - X)^{1/3} = K_c t$	Chemical reaction control dense constant size or shrinking spheres
$1 - (1 - X)^{2/3} + 2(1 - X) = K_c t$	Ash diffusion control dense constant size-spherical particles

a) Here, X, K_c, and t represent the fraction of metal ions (Li, Ni, Co) leached, the reaction rate constant in days, and the reaction time (days), respectively.

Table S2. Fitting parameters and relative contents of chemical species in XPS Ni 2p, Co 2p, Mn 2p, and O 1s spectra of spent NCM523 powder and the residues after incubation with gut microbiota.[b]

	Ni 2p	Ni(II)				Ni(III)			
		$2p_{3/2}$		$2p_{1/2}$		$2p_{3/2}$	$2p_{1/2}$	Satellite peak	
Spent NCM523 powder	BE (eV)	855.6		872.3		857.4	875.7	861.4	879.8
	Percentage	34.6%		18.0%		32.2%	16.3%	—	—
Residues	BE (eV)	855.7		873.7		857.9	875.9	861.0	879.5
	Percentage	40.9%		21.4%		28.6%	9.1%	—	—
	Co 2p	Co(II)				Co(III)			
		$2p_{3/2}$		$2p_{1/2}$		$2p_{3/2}$	$2p_{1/2}$	Satellite peak	
Spent NCM523 powder	BE (eV)	781.4		797.1		781.1	795.3	790.1	782.6
	Percentage	18.1%		9.5%		47.6%	24.8%	—	—
Residues	BE (eV)	782.6		798.3		781.1	796.9	786.2	803.1
	Percentage	33.7%		17.5%		32.3%	16.5%	—	—
	Mn 2p	Mn(II)		Mn(III)		Mn(IV)			
		$2p_{3/2}$	$2p_{1/2}$	$2p_{3/2}$	$2p_{1/2}$	$2p_{3/2}$	$2p_{1/2}$	Satellite peak	
Spent NCM523 powder	BE (eV)	—	—	642.1	653.4	643.5	654.9	638.9	—
	Percentage	—	—	40.8%	20.8%	25.7%	12.7%	—	—
Residues	BE (eV)	640.6	652.4	642.3	654.1			—	646.2
	Percentage	41.0%	20.9%	25.0%	13.1%			—	—

[b] "BE" and "Residues" stand for binding energy and residues after 22 days of incubation with gut microbiota, respectively.

Table S3. LCF results of Co and Mn *K*-edge spectra and goodness of fitting for residues after incubation with gut microbiota. (Data in parentheses represent three times the estimated standard deviation for each component derived from LCF fitting.[c] The R-factor indicates the mean-square misfit between the measured and modeled spectra.

Sample	Residues
Spent NCM523 powder (%)	0.1 (0.335)
CoO (%)	54.0 (0.598)
NH_4CoPO_4 (%)	19.8 (0.097)
$CoCO_3$ (%)	18.6 (0.135)
Co_3O_4 (%)	0 (0.866)
Co_2O_3 (%)	7.5 (1.12)
Reduced chi-square	0.0102
R-factor	0.0377
Spent NCM523 powder (%)	3.8 (0.036)
MnO (%)	1.9 (0.020)
$NH_4MnPO_4 \cdot H_2O$ (%)	43.8 (0.106)
$MnCO_3$ (%)	9.8 (0.043)
Mn_2O_3 (%)	30.7 (0.051)
MnO_2 (%)	7.5 (0.029)
Reduced chi-square	0.0001
R-factor	0.0006

[c] "LCF" stands for linear combination fitting.

Table S4. Dissolved mass of each metal ion in different spent LIB material systems, and the percentage of each material's total dissolved metal mass relative to its total metal mass at a powder mass of 0.4 g, a volume of 200 mL (corresponding to a pulp density of 2.0 g/L) on the 22nd day.[d)] Values in parentheses (mg) represent the theoretical values of metal ions in the corresponding systems.

Powder	**Li (mg)**	**Ni (mg)**	**Co (mg)**	**Mn (mg)**	**Al (mg)**	**Percentage**
NCM523	13.7 (14.8)	89.0 (116)	17.5 (43.6)	0.1 (59.7)	—	51.4%
NCA	4.4 (13.6)	12.8 (142)	3.0 (10.7)	—	0.2 (8.7)	12.1%
LCO	9.1 (13.7)	—	69.7 (226)	—	—	32.9%

[d)] Dissolution percentage = Total dissolved percentage (%) = $\left(\frac{\sum_{i=1}^{n} m_{i,dissolved}}{m_{total,theoretical}}\right) \times 100\%$, $\sum_{i=1}^{n} m_{i,dissolved}$: actual total dissolved mass of metal ions (mg); meaning the sum of the actual dissolved masses of all detected metal ions in the system (corresponding to the sum of the "dissolved masses of each metals" in the table). $m_{tatal,theoretical}$: theoretical total mass of metal ions (mg); meaning the theoretical total mass of all metal ions in the corresponding system (corresponding to the sum of the theoretical values of each metal ion in the parentheses in the table).

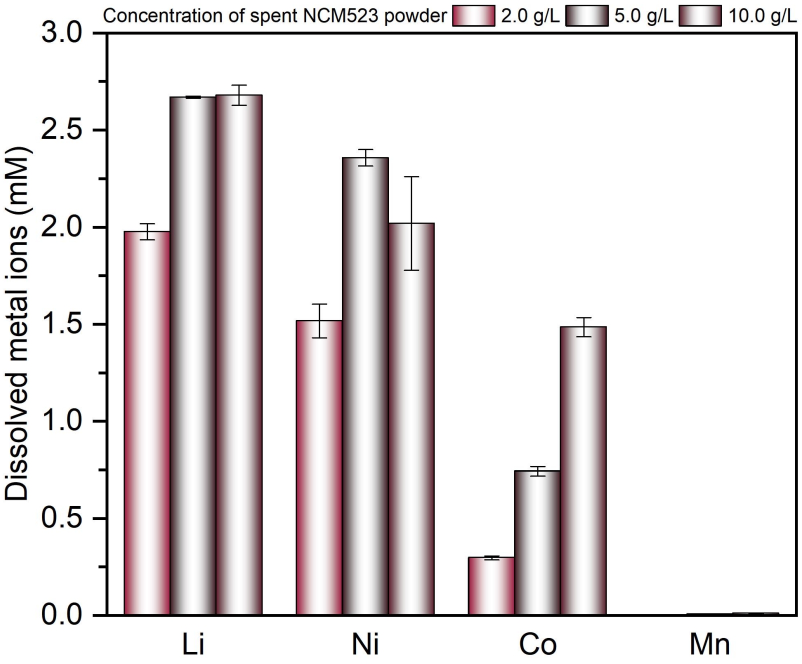

Fig. S1. Concentration of metals solubilized from different pulp densities of spent NCM523 powder after 22 days of incubation with gut microbiota. The results are the means and standard deviation of triplicate incubations.

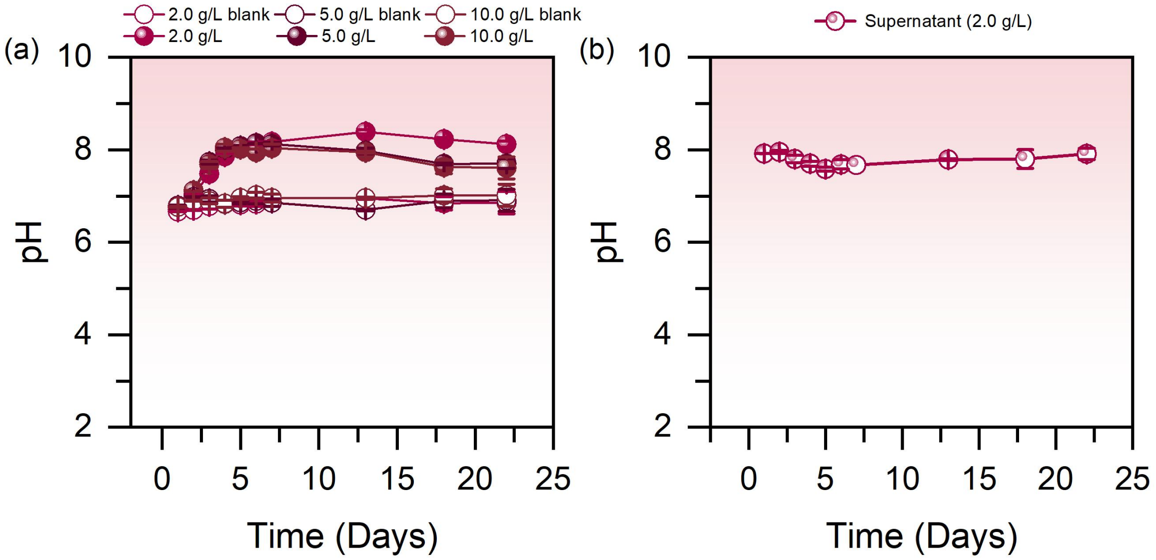

Fig. S2. Variations in culture medium pH during co-incubation of gut microbiota (**a**) or its culture supernatant (**b**) with spent NCM523 powder.

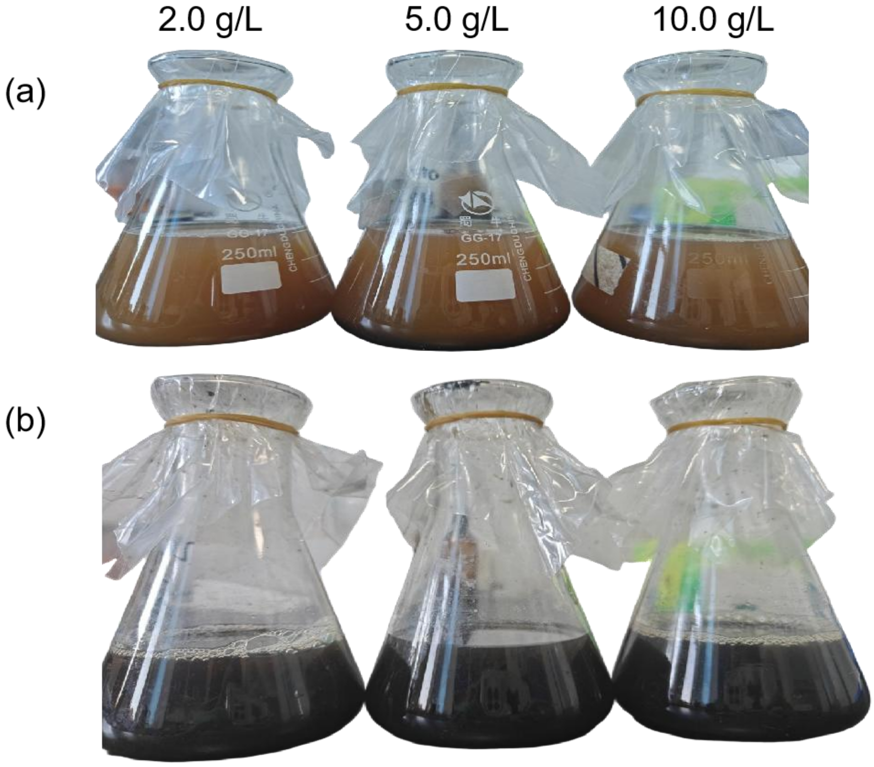

Fig. S3. Variations in culture medium color before (**a**) and after (**b**) incubation of gut microbiota with spent NCM523 powder. Experiments were performed in triplicates.

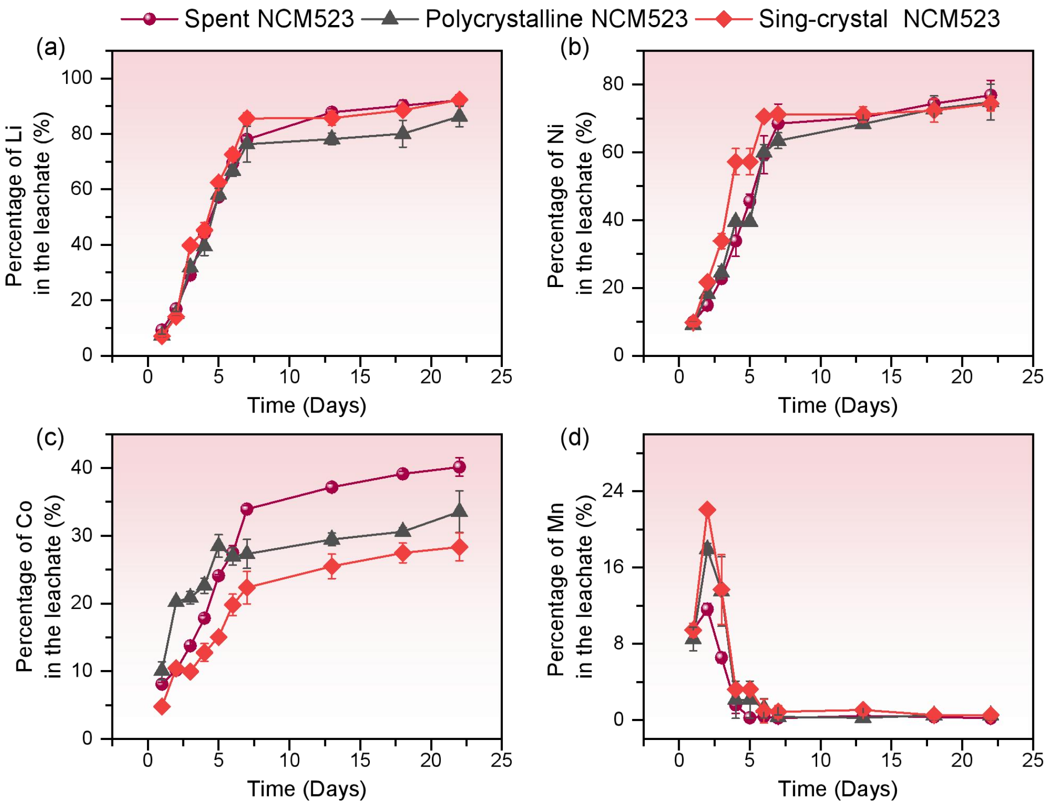

Fig. S4 Metal solubilization from polycrystalline NCM523 powder and single-crystal NCM523 powder (2.0 g/L) during co-incubation with gut microbiota. All results represent the means and standard deviations of triplicate incubations; the standard deviation range was smaller than the size of the data point symbols in some cases.

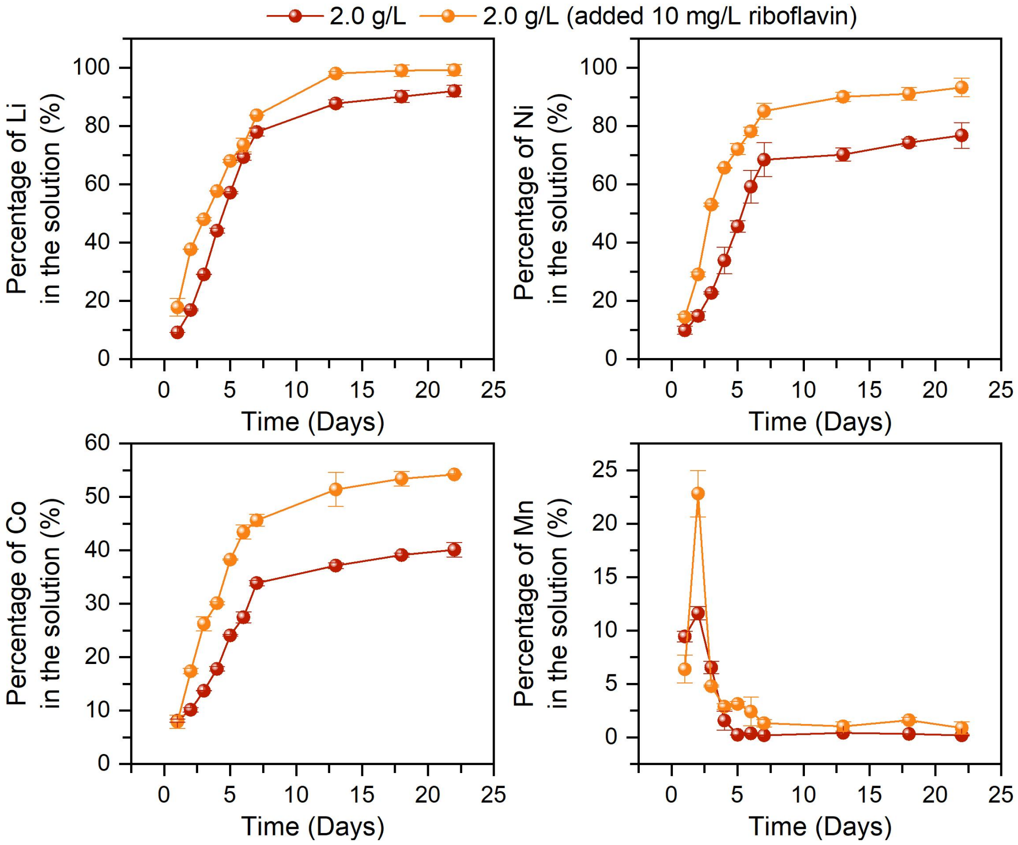

Fig. S5. Metal solubilization from spent NCM523 powder at a pulp density of 2.0 g/L by gut microbiota in the presence of 10 mg/L riboflavin. The results represent the means and standard deviations of triplicate incubations. In some cases, the standard deviation range was smaller than the data point symbol size.

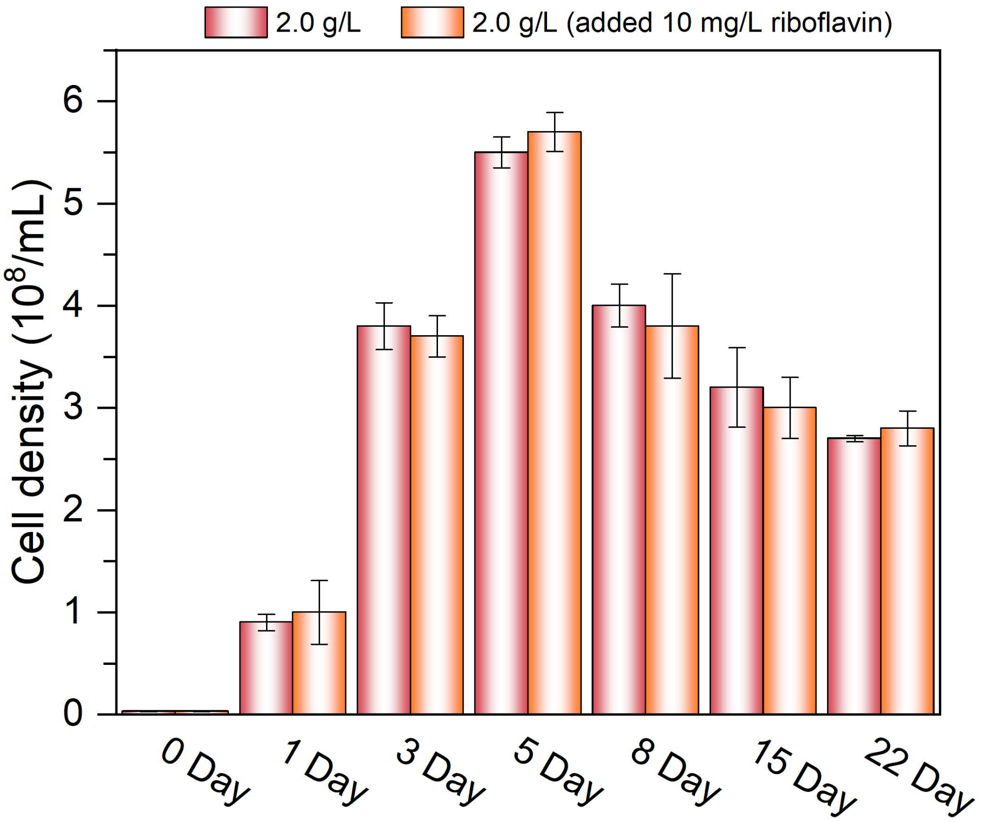

Fig. S6. Cell density from spent NCM523 powder at a pulp density of 2.0 g/L by gut microbiota in the absence and presence of 10 mg/L riboflavin. Cell counts were determined using the dilution plate-count method on solid BHI medium (as described in the main text) supplemented with 2 % agar powder. The results represent the means and standard deviations of triplicate incubations.

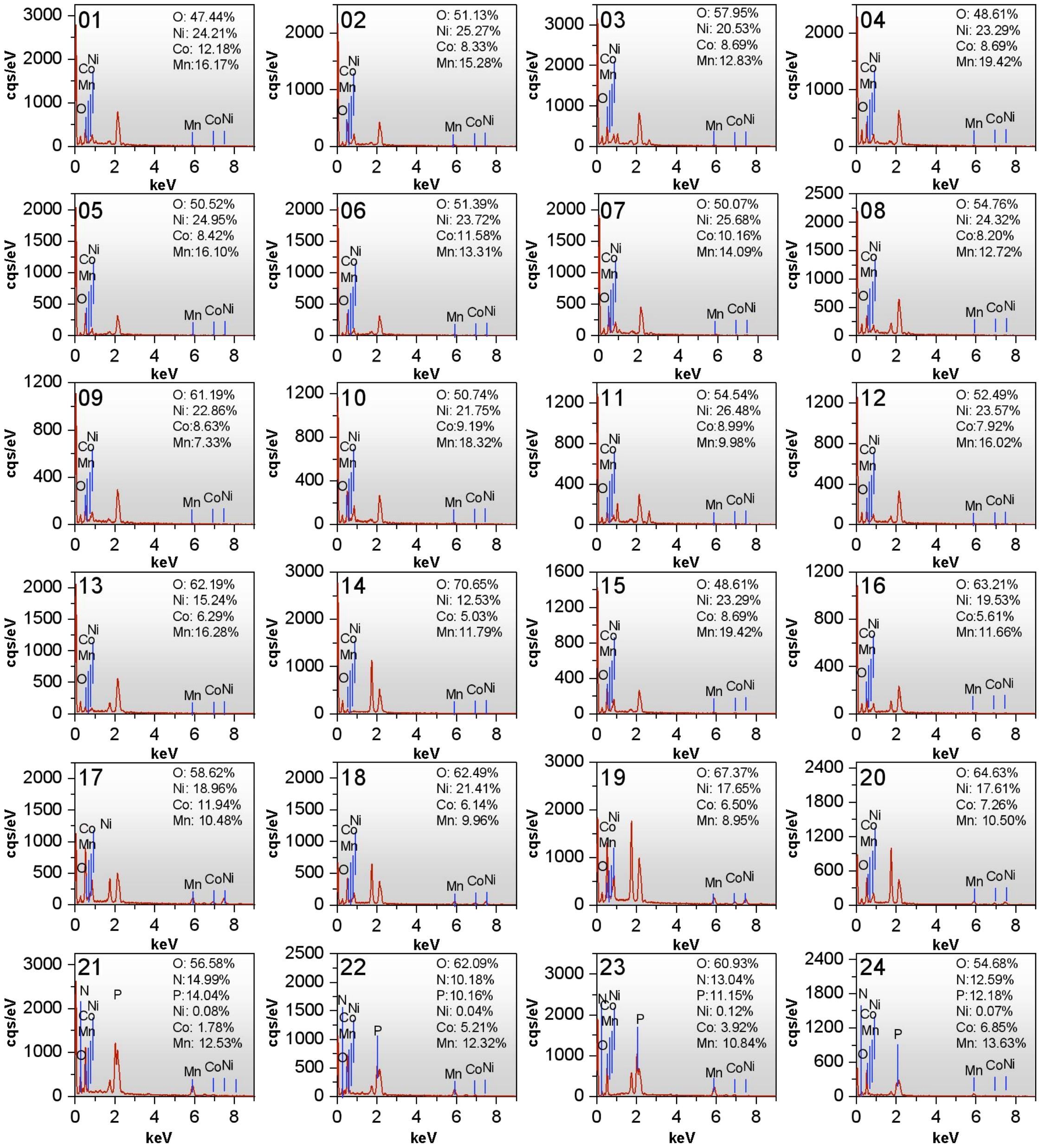

Fig. S7 EDS results corresponding to the positions marked with "01–24" red crosses in Fig. 4.

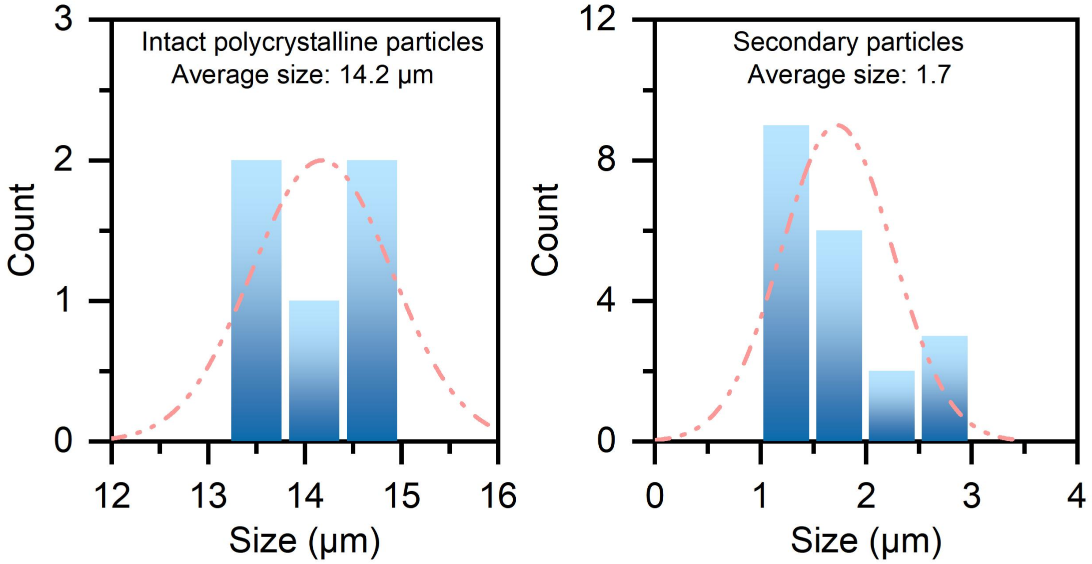

Fig. S8 The particle size statistics were performed using ImageJ 1.53 software, with the statistical data derived from the SEM image in Fig. 4a.

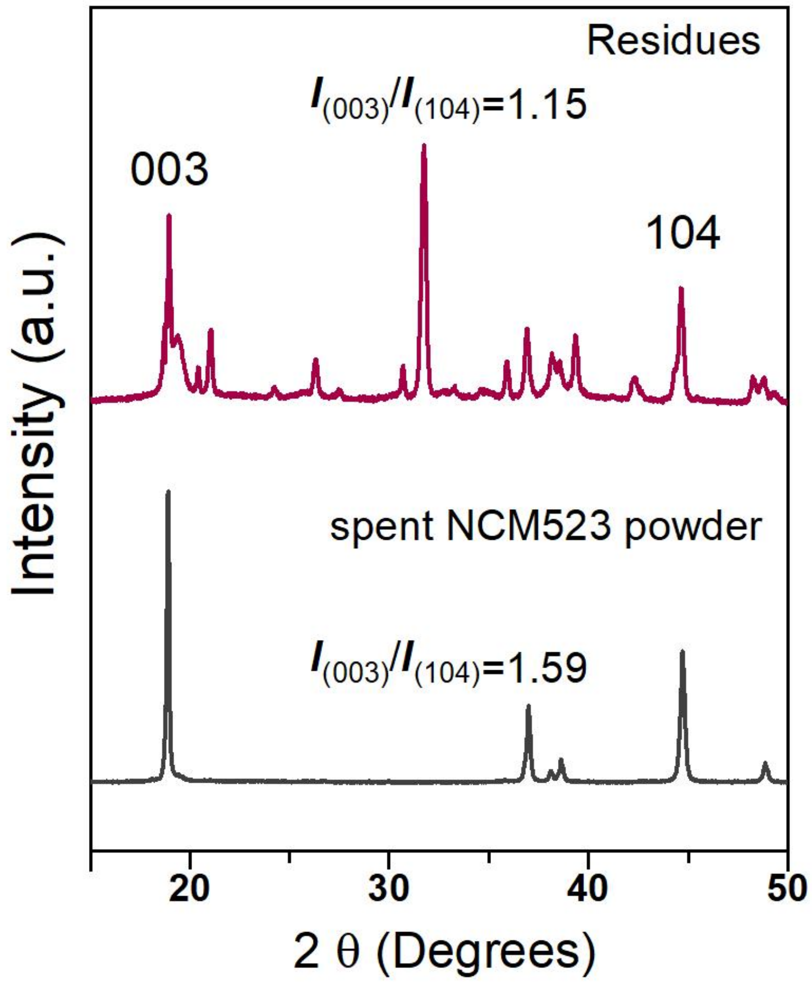

Fig. S9 XRD patterns of the samples of residues after bioleaching using gut microbiota.

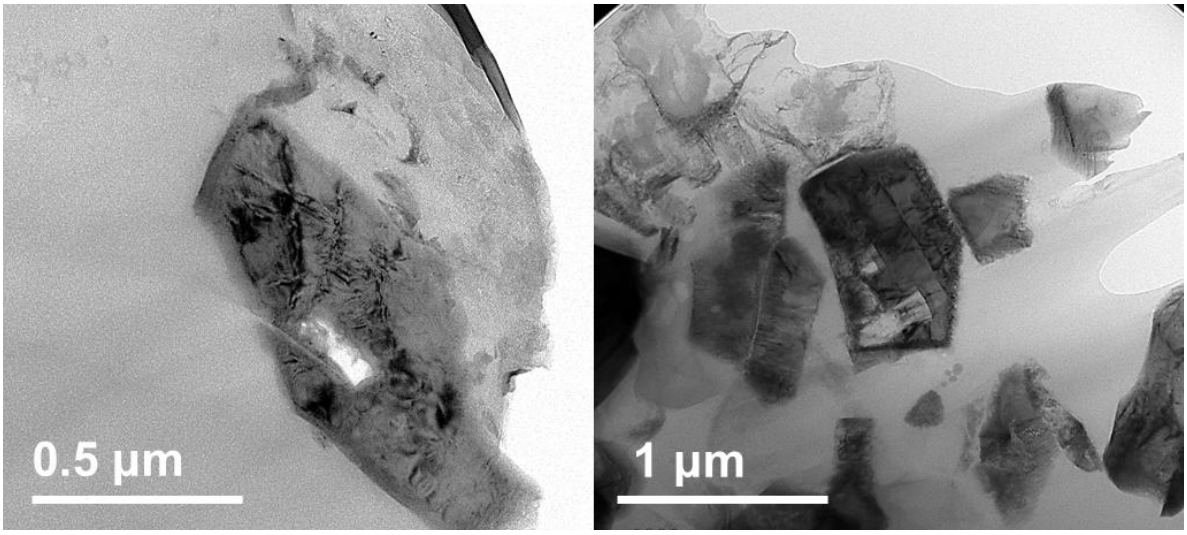

Fig. S10 Bright-field TEM images of the residue particles with internal developed from the bacterial attack after 3 days of bioleaching.

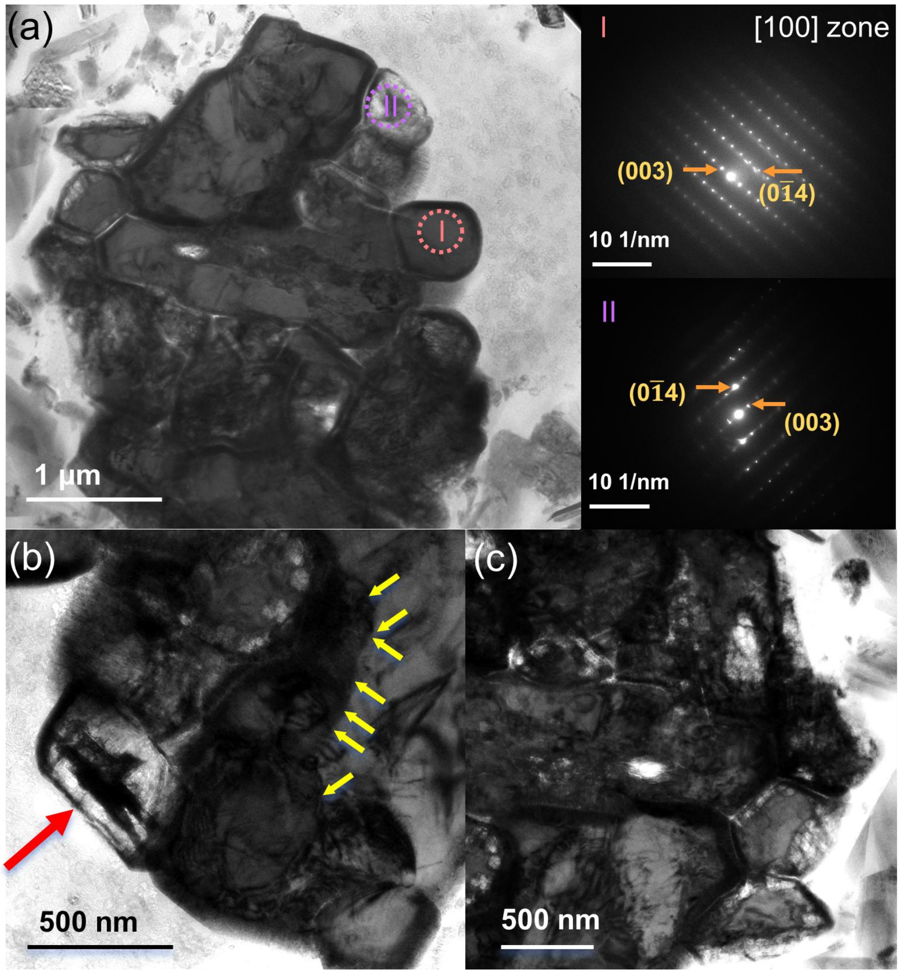

Fig. S11 A bright-field TEM image of polycrystalline residue particle after bioleaching for 22 days. (**a**) The residue particle, a remnant of a fractured secondary cathode particle, retained a polycrystalline structure, consisting of 10−20 primary particles. A selected area electron diffraction (SAED) pattern from a particle (labelled I) reproduces a [100] zone diffraction of the layer structure with no streaks and satellite spots, indicating that this grain is preserved from the bacterial attack. In contrast, a SAED pattern from a particle labelled II shows no high-order diffraction peaks and a strong set of $(0\bar{1}4)$ spots, suggesting severe deterioration of the crystal structure. However, the presence of the (003) spots confirms that the layered structure framework is still maintained in this primary particle. (**b**) A magnified image shows a grain that is nearly transparent due to material loss (red arrow) and the development of a sub-grain boundary at an incipient stage of grain breakup (yellow arrows). (**c**) A series of voids along grain boundaries and large internal voids are observed.

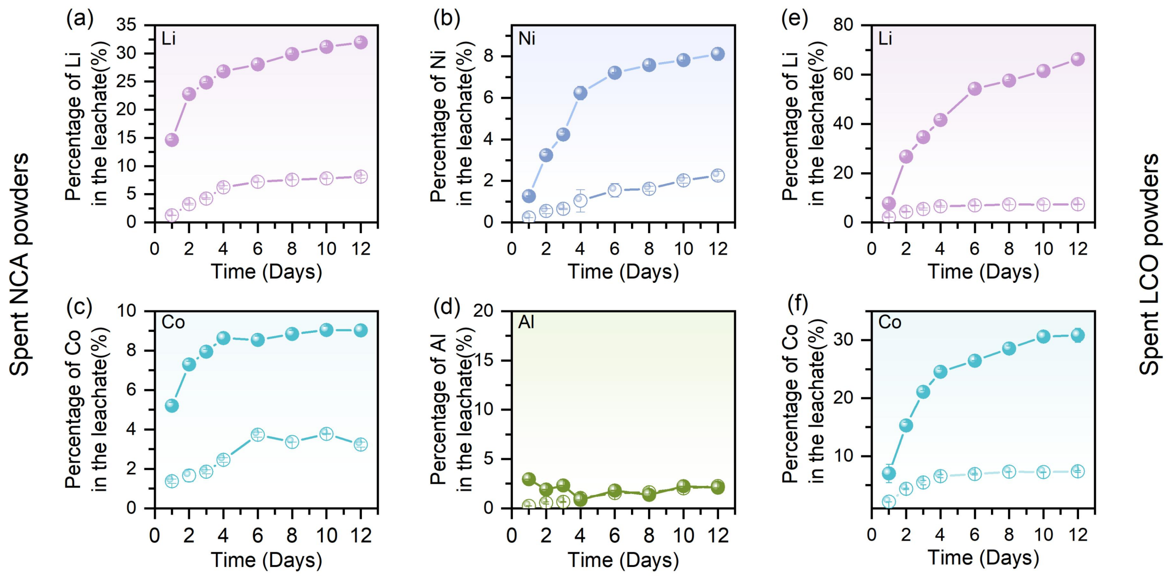

Fig. S12 Metal solubilization from spent NCA and LCO powder at a pulp density of 2.0 g/L incubated with gut microbiota. The results represent the means and standard deviations of triplicate incubations. In some cases, the standard deviation range was smaller than the data point symbol size.

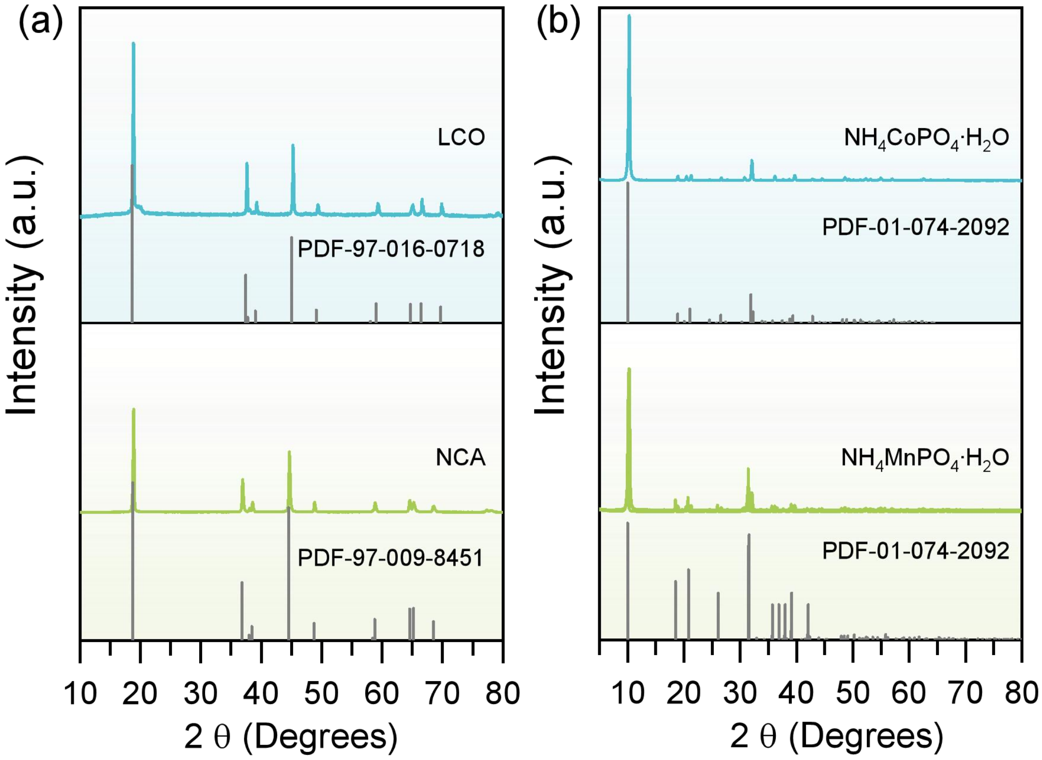

Fig. S13 XRD patterns of $NH_4CoPO_4 \cdot H_2O$, $NH_4MnPO_4 \cdot H_2O$, untreated spent NCA, and LCO cathode powder. "NCA" and "LCO" stand for $LiNi_{0.8}Co_{0.15}Al_{0.05}O_2$ and $LiCoO_2$, respectively.

References

1. Wang, X. et al. $NH_4CoPO_4 \cdot H_2O$ Microflowers and Porous $Co_2P_2O_7$ Microflowers: Effective Electrochemical Supercapacitor Behavior in Different Alkaline Electrolytes. *Int. J. Electrochem. Sci.* **8**, 3768−3785 (2013).
2. Pang, H. et al. Template-free Controlled Fabrication of $NH_4MnPO_4 \cdot H_2O$ and $Mn_2P_2O_7$ Micro-Nanostructures and Study of Their Electrochemical Properties. *Int. J. Electrochem. Sci.* **7**, 12340−2353 (2012).
3. Zhang, C. et al. New method for the preparation of hierarchical nanotube $K_{0.3x}Mn_xCe_{1-x}O_\delta$ catalysts and their excellent catalytic performance for soot combustion. *Appl. Catal. B: Environ. Energy* **355**, 124169 (2024).
4. Zhu, Y. et al. Enhanced performance of carbon dots and Mn_3O_4 composite by phosphate in peroxymonosulfate activation. *Appl. Catal. B Environ.* **351**, 123954 (2024).
5. Li, S. et al. Highly efficient anion exchange membrane water electrolyzers via chromium-doped amorphous electrocatalysts. *Nat. Commun*. **15**, 3416 (2024).
6. Kühn, T. J. et al. Site-selective high-resolution X-ray absorption spectroscopy and high-resolution X-ray emission spectroscopy of cobalt nanoparticles. *Inorg. Chem.* **53**, 8367−8375 (2014).
7. Phumying, S. et al. Synthesis, characterization, magnetic and ion release properties of $NH_4MPO_4 \cdot H_2O$ (M= Mn^{2+}, Fe^{2+}, Co^{2+}, Cu^{2+}) prepared by a simple precipitation method in water solution. *Appl. Phys. A* **127**, 352 (2021).
8. Farges, F. Ab initio and experimental pre-edge investigations of the Mn *K*-edge XANES in oxide-type materials. *Phys. Rev. B: Condensed Matter and Materials Physics* **71**(15), 155109 (2005).
9. Zhang, W., et al. Efficient Detection of Low-Content Diamond Crystals in Sand via X-ray Powder Diffraction: A Guided-Inquiry Instrumental Analysis Laboratory Experiment. *J. Chem. Educ.* **101**, 4411−4416 (2024).
10. Whitaker, A. The Value of X-ray Powder Diffraction Analysis in Colour Chemistry. *J. Soc. Dyers Colour.* **102**, 66−76 (1986).
11. Singh, N. *et al.* Hydrometallurgical Approach to Recover Vanadium and Aluminum from the Sulfuric Acid Manufacturing Spent Catalyst. *Miner. Process. Extr. Metall. Rev.*, 1−12 (2025).
12. Singh, N. et al. Recovery of aluminum, vanadium, and nickel from waste desulfurization catalyst residue by roasting and water leaching. *J. Ind. Eng. Chem.* **143**, 632−644 (2025).